FILAMENTATION INSTABILITY OF A RELATIVISTIC ELECTRON BEAM IN A FOIL TRANSPORT CHANNEL

S. HUMPHRIES, JR.

Department of Electrical and Computer Engineering, University of New Mexico, Albuquerque, New Mexico 87131

and

CARL EKDAHL

Los Alamos National Laboratory, Los Alamos, New Mexico 87545

High-current relativistic electron beams can be focused in vacuum by arrays of transverse conducting foils. The foils reduce defocusing space-charge electric fields, allowing self-pinched propagation. Beams in such a transport channel may be subject to a filamentation instability caused by local magnetic pinching; similar processes are observed when high-current electron beams pass through a neutralizing plasma. The instability leads to a growth of the beam emittance. We report observations of the filamentation of a 4-kA, 280-keV electron beam propagating in a transport array of fine wire meshes. Strong modulation of the beam density was observed with propagation lengths of only a few centimeters. Observations of the filamentation of a sheet beam are compared to a theoretical model that accurately predicts the instability growth length and saturation values of beam angular divergence. The filamentation instability is not expected to be a serious problem for paraxial beam transport. However, the present results indicate that filamentation may degrade the quality of intense relativistic electron beams generated by high-perveance guns with an anode foil.

1. INTRODUCTION

Filamentation instabilities are a familiar phenomenon in the transport of intense relativistic electron beams in plasmas.[1–9] When the space-charge electric field of a relativistic beam is canceled, transverse nonuniformities of current density can grow because of local pinching by the strong beam-generated magnetic fields. In this paper, we report observations of transverse filamentation of 280-keV electron beams propagating in high vacuum. The beams were transported in a self-focused mode using transverse conducting foils.[10–13] The presence of magnetic filamentation is not surprising since the purpose of the foils is to reduce space-charge electric fields to allow a self-contained equilibrium. Foil transport achieves space-charge neutralization with image charges, whereas plasma neutralization results from free charges. With regard to the filamentation instability, the final state is not strongly affected by the neutralization method.

The magnetic filamentation instability reaches saturation when the beam gains sufficient dispersion in transverse velocity. Ultimately, the transverse beam-

pressure force becomes large enough to resist magnetic pinching. The end result of filamentation is growth of the beam emittance. The results reported in this paper suggest limitations on the quality of beams in space-charge-neutralized transport systems and suggest optimal approaches to limit emittance growth. The results also bear on the feasibility of relativistic electron guns with anode grids or foils. We observed strong beam filamentation in various gun geometries within a few centimeters of an anode mesh.

Experimental observations of the filamentation of a high-perveance beam from a 4-kA, 280-kV electron gun are described in Section 2. In addition to performing voltage and current diagnostics, we measured time-integrated output beam profiles and emittances. Circular and annular cathodes were used with a fine mesh anode. Filamentation of annular beams was particularly violent; beam electrons developed an azimuthal divergence angle of ±15° within 2–4 cm of the anode. Measurements of the transverse distribution of current density showed complex structures for both guns. To compare experimental results with theoretical predictions, we designed a cathode to generate a well-confined thin-sheet beam. Experimental results on filamentation of sheet beams are reported in Section 4; a simplified theoretical treatment for the beam geometry is developed in Section 3. Measured values of the instability growth length, instability wavenumber, and saturation angular divergence are in good agreement with the theory. Implications of the results for foil transport are discussed in Section 5.

2. OBSERVATIONS OF FILAMENTATION INSTABILITIES IN CYLINDRICALLY SYMMETRIC BEAMS

The pulsed electron gun was driven by a CHAC generator.[14] The water-filled Blumlein line produced a 60-ns (full width at half-maximum) pulse with a good 40-ns flattop. The pulse line, electron gun, and transport volume are illustrated in Fig. 1. We modified the output section of the pulse line, incorporating a large output resistor and radial vacuum insulator. The resistor was used in place of an inductor to relieve charge from the Blumlein-line center conductor during pulsed energy transfer from the Marx. Although the resistor caused a relatively high positive prepulse voltage (~60 kV) on the gun cathode, we encountered no problem with premature emission. In contrast to the situation with an inductor, the prepulse-voltage waveform wth a resistor was monopolar; the positive cathode prepulse voltage inhibited electron emission. The output-voltage waveform was optimized by adjusting the output resistor to match the net load impedance. The resistor also served to absorb postpulse energy, so that we were able to accumulate a large number of shots on the gun with no damage to the fine anode mesh.

The gun voltage was measured using a balanced probe in the output resistor (Fig. 1). The monitor was cross-calibrated against a magnetic spectrometer that measured the electron output energy. The slow rise time of the beam current in the diode contributed an inductive correction to the voltage monitor signal of less than 10 kV, or less than 5%. The current of the extracted electron beams was
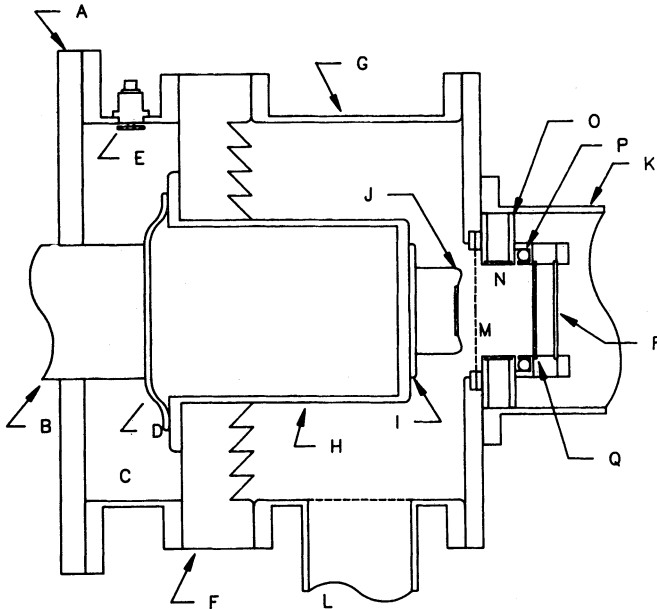
FIGURE 1 Experimental system: (A) pulser output insulator; (B) high-voltage output terminal, 300-kV pulser; (C) Blumlein line shunt resistor, aqueous resistive solution; (D) flexible contacts; (E) balanced voltage monitor; (F) radial vacuum insulator; (G) vacuum chamber; (H) high-voltage terminal; (I) adjustable cathode carrier; (J) surface plasma cathode with focusing electrode; (K) transport tube; (L) vacuum-pump port; (M) mesh anode; (N) transport-system spacer rings; (O) transport-system support flange; (P) shielded current monitor; (Q) pepperpot aperture plate; (R) coated scintillator sheet.

typically 4 kA or less. Beam current extracted through the anode and transported in vacuum by foil arrays was measured with calibrated in-vacuum current monitors. The monitors (Fig. 1) contained a toroidal multiturn Rogowski coil[15,16] in a re-entrant shield. The coil was potted in low-vapor-pressure epoxy. The predicted rise time of the current monitors was 5 ns.[17] Oscillograph traces of cathode voltage and extracted electron current for the planar gun described in Section 4 are shown in Fig. 2. Although the voltage was constant over the pulse
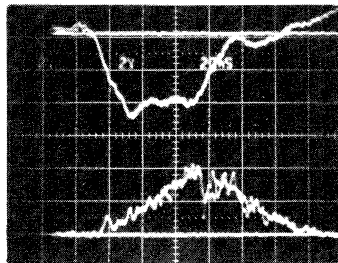

FIGURE 2 Cathode voltage and extracted current, planar gun with focusing electrode, 1.3-cm cathode-anode gap spacing. Top: gun voltage, 120 kV/div, 20 ns/div. Bottom: beam current 1.5 cm from anode grid, 1.22 kA/div, 20 ns/div.

length, the current exhibited a long-term increase. Variation of the current was probably a consequence of plasma expansion from the cathode.

Electrons were generated from an explosive plasma cathode activated by the extraction voltage pulse. We used velvet cloth as the active surface; this fabric ignites rapidly and produces a uniform electron beam.[18,19] We used a variety of cathode geometries. In most cases, the velvet surface was surrounded by a modified Pierce focusing electrode,[20] as shown in Fig. 1. The polished stainless-steel electrode inhibited edge emission and aided in the creation of well-directed beams. Measurements of the extracted beam profiles confirmed that, when the field stress on the focusing electrode was less than 300 kV/m, electrons were emitted only from the velvet surface. The anode consisted of a planar mesh composed of 0.0025-cm-diameter stainless-steel wires with a transparency of 80%. The current at the end of the voltage pulse was about double the space-charge limit,[21] implying that the width of the extraction gap was reduced by a factor of 0.7 at the end of the pulse. This figure implies a plasma expansion velocity of about 10 cm/μs, a typical value for surface-plasma cathodes operated at high current density (100–200 A/cm^2).[22]

The time-integrated beam profile was measured by taking open-shutter photographs of a scintillator surface, coated with graphite, that intercepted the beam. Multiple layers of fine mesh were compressed against the entrance surface to attenuate the beam and relieve charge accumulation. The time-integrated beam emittance was measured using the "pepperpot" illustrated in Fig. 1.[23] For these measurements, the scintillator sheet was located 1.4 cm behind an aperture plate. The 0.05-cm-thick stainless-steel aperture plate had an array of 0.04-cm-diameter holes 0.5 cm apart.

Electron beams were transported through removable foil assemblies inserted into a 20.3-cm-diameter cylindrical vacuum chamber. To propagate the 280-keV electron beam through large numbers of focusing cells, wire meshes were used instead of foils. The meshes, constructed from 0.005-cm-diameter wires mounted on a mandrel, had 98% transparency. As shown in Fig. 1, a variety of cell geometries could be achieved by stacking spacers and meshes. The transport assembly had an inner diameter of 9.6 cm. The current monitor and emittance diagnostics were usually mounted at the end of the system.

We first observed evidence of filamentation using the high-perveance cylindrical cathode with focusing electrode illustrated in Fig. 3a. The active cathode surface was 5.1 cm in diameter, and the initial width of the cathode-anode gap was 2.0 cm. The extracted current reached a value of 2.6 kA at the end of the voltage pulse, corresponding to 3.3 kA of electron flow in the cathode-anode gap. The final current was about 1.8 times the space-charge limit, implying a final effective gap width of 1.5 cm. Beam-profile measurements were performed with a detector 4.5 cm from the anode mesh.

The measured beam profile is illustrated in Fig. 4a. The time-integrated photograph shows a clear indication of beam filamentation; the beam edge was strongly feathered, the result of local electron pinches and orbit crossings. The observed beam radius was substantially larger than the cathode radius. There are

(a)

Focusing electrode

Cathode

Anode mesh

|——————|
10 cm

(b)

Cathode support

Annular cathode
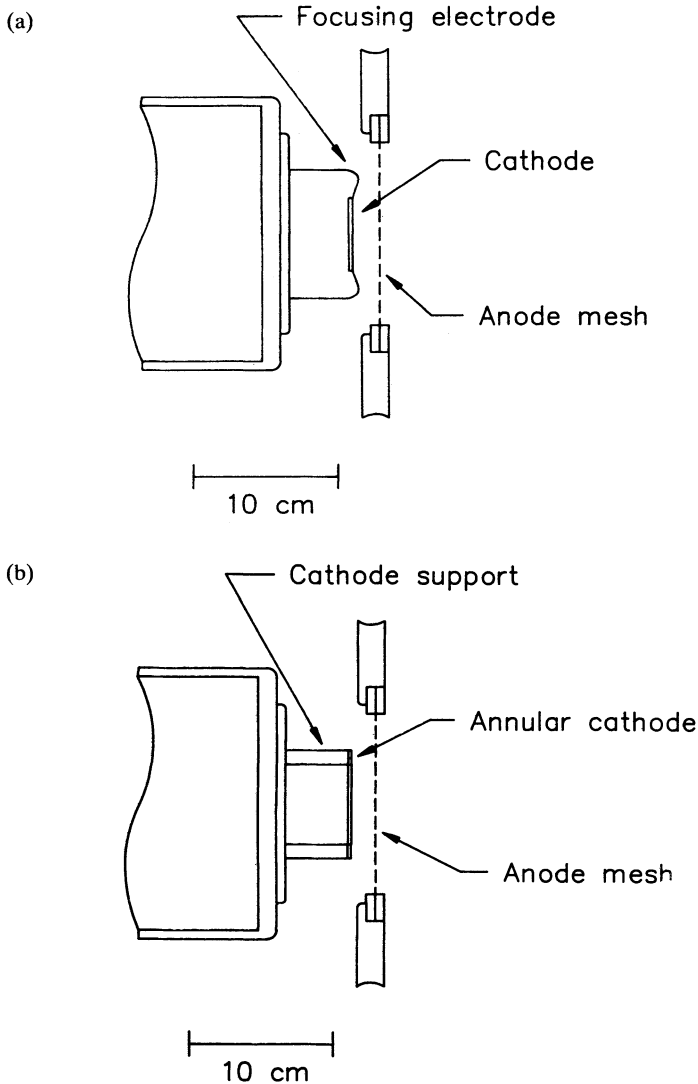
Anode mesh

|——————|
10 cm

FIGURE 3   Electron-gun geometries: (a) high-perveance circular cathode with focusing electrode and (b) simple annular cathode.

three potential causes for enlargement of the beam:

1. The exposure of the profile photograph was strongest at the end of the pulse, when the beam current was enhanced by plasma closure. The higher current caused increased space-charge expansion in the propagation region.

2. Plasma expansion moved the emission surface away from the physical cathode surface, degrading the gun optics.

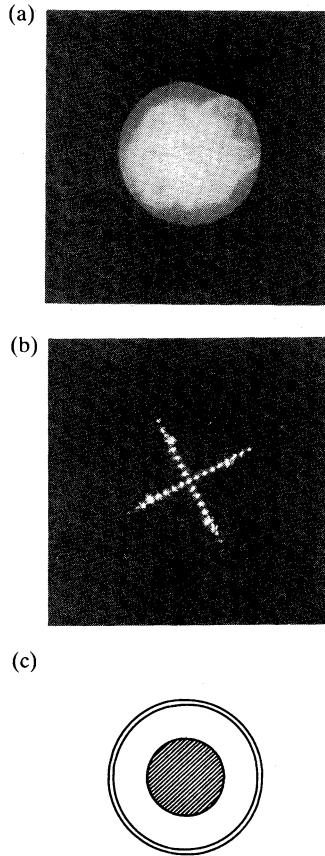3. Filamentation caused significant disordered transverse motions of electrons.

FIGURE 4 Output-beam properties, high-perveance circular cathode: (a) beam spatial profile, 2-cm cathode-anode gap, scintillator 4.5 cm downstream from anode mesh; (b) emittance measurement, 1.7-cm cathode-anode gap, aperture plate 3.8 cm downstream from anode mesh; and (c) scale drawing of cathode and transport-tube cross sections.

Effects of the filamentation instability on the beam distribution are illustrated in the pepperpot data of Fig. 4b. Analysis of the centroid locations shows that the beam diverged with an angle of about 8° at a 2.5-cm radius. An inspection of the shape of the spots shows a complex angular structure. The divergence angle of electron orbits was approximately isotropic in the radial and azimuthal directions. The approximate boundary value of the divergence angle is plotted in Fig. 5 as a function of radial position. The greatest increase in angular divergence occurred on the periphery of the beam; the average divergence angle was about 7.5°.

We observed interesting filamentary behavior using the annular cathode illustrated in Fig. 3b. The cathode was a simple velvet annulus with no focusing electrode. The cathode proved useless for propagation experiments because
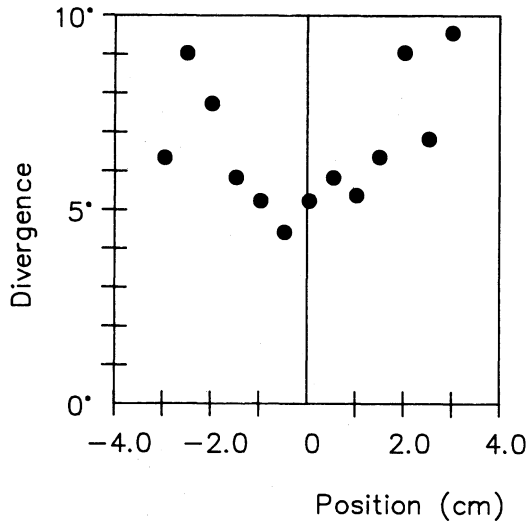
FIGURE 5   Linear scan of angular divergence across beam, 3.8 cm from anode mesh [reduction of Fig. 4(b)]. High-perveance circular cathode, 1.7-cm cathode-anode gap.

emission was dominated by edge effects; the resulting beam had strong divergence radially inward and outward from the initial annulus. The most significant result from experiments with the ring cathode was the occurrence of a strong filamentation instability. The initially thin sheet beam pinched into a number of bunches, resulting in a large increase in disordered azimuthal velocity.

Because of edge emission, the net current from the 20-cm^2 cathode was substantially higher than the planar space-charge limit prediction at all times. With a 1.7-cm gap, the peak current was typically 4.5 kA. A beam profile measured 1.7 cm downstream from the anode is shown (as a) in Fig. 6. A scale drawing of the cathode dimensions is included (as c) in Fig. 6. The effect of azimuthal filamentation superimposed on radial expansion of the beam is evident. The emittance plot (b) of Fig. 6 shows strong angular beam clumping in the azimuthal direction. Although the average radial beam divergence angle was only ±5.7°, the azimuthal divergence was ±15.4°. This angular divergence was acquired within a propagation distance of less than 3 cm.

3. SCALING LAWS FOR SHEET-BEAM FILAMENTATION

Although the beam filamentation described in Section 2 resulted from straightforward magnetic pinching, analysis of the process is difficult because of the three-dimensional geometries involved. To carry out a quantitative investigation of the factors affecting the growth of filaments, we designed a cathode to generate a parallel sheet beam. Experimental results on the thin one-dimensional beam geometry are described in Section 4. The linear theory of thin-beam filamentation in a foil focusing system is reviewed in this section. The theory gives first-order estimates of growth rates and saturation values of beam divergence that are in good agreement with experimental observations.
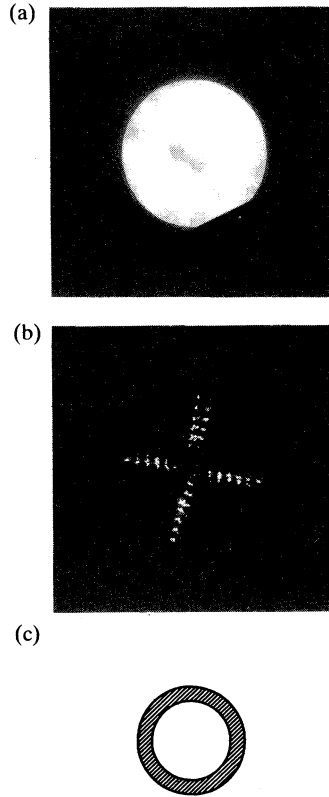
(a)

(b)

(c)

FIGURE 6 Output-beam properties, annular cathode: (a) beam spatial profile, 1.7-cm cathode-anode gap, scintillator 1.7 cm downstream from anode grid; (b) emittance measurement, 1.7-cm cathode-anode gap, aperture plate 1 cm downstream from anode mesh; and (c) scale drawing of annular cathode.

A thin-sheet beam is illustrated in Fig. 7. The beam propagates in the z-direction; it is assumed that the beam has infinite extent and uniform properties in the direction of propagation. In equilibrium, the beam is uniform in the x-direction; we shall investigate conditions under which perturbations in the x-direction lead to magnetic pinching. In the experiments, the beam propagates through a number of closely spaced transverse meshes. The meshes reduce space-charge effects but have little effect on magnetic fields. The experimental geometry, with its axial variations, is difficult to describe analytically. Instead, we shall concentrate on the simplified geometry of Fig. 7. The beam is contained between symmetric planar boundaries. To model the effect of partial space-charge neutralization by transverse foils, the image-charge boundary is located at a different position than the image-current boundary. The image-charge boundary at position $\pm y_e$ with respect to the beam axis defines a surface of constant electrostatic potential, ϕ, where $E_x = 0$. The return-current boundary at position $y_m \geq y_e$ defines a surface of constant vector potential, A_z, where $B_y = 0$.
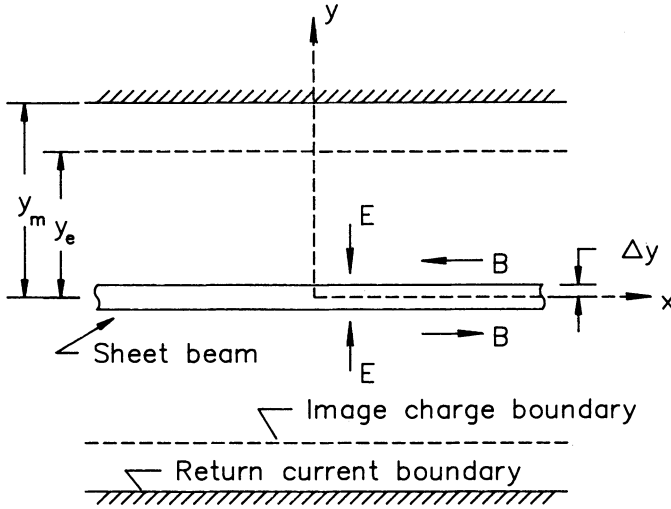
FIGURE 7   Geometric parameters, filamentation of a thin-sheet beam.

To facilitate a linear analysis of beam stability, we assume that the relativistic sheet beam satisfies the paraxial approximation, v_x, $v_y \ll v_z$. This condition implies that all beam electrons have about the same kinetic energy, $(\gamma - 1)m_0 c^2$, and longitudinal velocity, $v_z \cong \beta c$. Transverse motion can be described by equations in a nonrelativistic form with an adjusted particle mass, γm_0. Unspecified equilibrium forces act to confine the beam in the y-direction; we shall consider only the possibility of motion in the x-direction. In the equilibrium state, the beam is taken to have uniform charge density ρ_0 distributed over a half-thickness Δy. The thin-beam limit is described by the condition $\Delta y \ll y_e$, y_m. Perturbations in the x-direction are taken to have a scale length that is long compared to the beam thickness. In terms of the spatial wavenumber, k, this condition can be expressed as $k \leqslant 1/\Delta y$. The quasi-static approximation is applied to estimate the electric and magnetic fields; this limit is valid if instability growth times are long compared to $1/kc$.

In equilibrium, the electric and magnetic fields have the following values at the beam boundaries:

$$E_{y0} = \pm \rho_0 \Delta y / \varepsilon_0, \tag{1}$$

$$B_{x0} = \pm \mu_0 \rho_0 \Delta y \beta c. \tag{2}$$

We assume a perturbation of beam charge density in the x-direction with wavenumber k:

$$\rho(x) = \rho_0 + \Delta \rho \cos kx. \tag{3}$$

The density variation gives rise to an associated perturbation of beam current density:

$$j_z(x) = \rho_0 \beta c + \Delta \rho \beta c \cos kx. \tag{4}$$

To begin, we shall calculate the electrostatic potential associated with the perturbed density. The solution that satisfies Laplace's equation outside the beam and meets the boundary condition at the conducting boundary is

$$\Delta\phi(x, y) = \Delta\phi_k \cos(kx)[\exp(ky)\exp(-ky_e) - \exp(-ky)\exp(ky_e)]. \quad (5)$$

There is an additional matching condition for the electric field at the beam boundary. In the limit that $\Delta y \to 0$, the normal component of the electric field approaches the value:

$$\Delta E_y(0^+) = -\partial\phi(x, 0)/\partial y = \Delta\rho\Delta y \cos(kx)/\varepsilon_0. \quad (6)$$

Equation (6) implies that

$$\Delta\phi_k = -(\Delta\rho\Delta y/4\varepsilon_0)\cosh(ky_e). \quad (7)$$

The electric-field component E_x affects the growth of filamentation instabilities. Taking $\Delta E_x = -\partial\phi(x, y)/\partial x$ yields the following expression:

$$\Delta E_x(x, y) = (\Delta\rho\Delta y/2\varepsilon_0)\tanh(ky_e)\sin(kx). \quad (8)$$

A similar treatment can be applied to calculate the perturbed magnetic field. A solution for the vector potential $A_z(x, y)$ yields the result:

$$\Delta B_y(x, y) = (\Delta\rho\Delta\beta/2\varepsilon_0 c)\tanh(ky_m)\sin(kx). \quad (9)$$

The net force in the x-direction resulting from perturbed beam-generated fields is

$$F_x = (e\Delta\rho\Delta y/2\varepsilon_0)\sin(kx)[\tanh(ky_e) - \beta^2\tanh(ky_m)]. \quad (10)$$

The linearized moment equations for beam motion in the x-direction are

$$\frac{\partial\Delta\rho}{\partial t} + \frac{\partial}{\partial x}(\rho_0\Delta v_x) = 0 \quad (11)$$

and

$$\gamma m_0\rho_0\frac{\partial\Delta v_x}{\partial t} + \gamma m_0\langle\delta v_x^2\rangle\frac{\partial\Delta\rho}{x} = \frac{\rho_0 e\Delta y}{2\varepsilon_0}\Delta\rho\sin(kx)[\tanh(ky_e) - \beta^2\tanh(ky_m)]. \quad (12)$$

The quantity Δv_x is the perturbed directed velocity, whereas $\langle\delta v_x^2\rangle$ represents a random velocity dispersion in the x-direction. With the assumption that all quantities vary as $\exp(\alpha t)\sin(kx)$, Eq. (12) reduces to the following expression for the linear growth rate of perturbations:

$$\alpha^2 = -k^2\langle\delta v_x^2\rangle - (eJ_z/2\gamma m_0\beta c\varepsilon_0)k\tanh(ky_e)$$
$$+ \beta^2(eJ_z/2\gamma m_0\beta c\varepsilon_0)k\tanh(ky_m). \quad (13)$$

The quantity J_z is the net current of the equilibrium beam per unit length along x:

$$J_z = en_0\Delta y\beta c. \quad (14)$$

The beam pressure and space-charge force have a stabilizing effect, whereas the beam-generated magnetic force leads to growth of perturbations. The beam is stable if $y_e = y_m$; in this case, the repulsive electric forces dominate. The effect of

adding transverse foils for focusing can be simulated by taking $y_e < y_m$. In this case, the transverse electric field is reduced more than the magnetic field, and a low-emittance beam may be subject to a pinching instability. The result of the instability is to increase the transverse emittance of the beam. Ultimately, the transverse beam velocity dispersion grows to a level that stabilizes pinching. The root-mean-squared beam angular dispersion for stable propagation is given by

$$\Delta \theta \cong \frac{(\langle \delta v_x^2 \rangle)^{1/2}}{\beta c} = \left\{ \frac{(qJ_z)[\beta^2 \tanh (ky_m) - \tanh (ky_e)]}{(2\varepsilon_0 \gamma m_0 \beta^2 c^3)k} \right\}^{1/2}. \tag{15}$$

4. OBSERVATION OF SHEET-BEAM FILAMENTATION

We conducted experiments using a sheet-beam cathode to clarify the nature of the high-vacuum filamentation instability and to verify the theoretical predictions of Section 3. The active area of the plasma-emission cathode was 0.5 cm wide by 8.5 cm long. Along the length, the emission area was bordered by polished stainless-steel focusing electrodes. A cross section of the gun with a simulation of sheet-beam extraction using the EGUN code[24] is shown in Fig. 8. The simulation predicts a linear current density of 8.5 kA/m in the anode-cathode gap. For propagation experiments, we could arrange a wide variety of foil-transport geometries, such as the three-cell system illustrated in Fig. 8. Most instability measurements were performed with the diagnostic package as close as possible to the anode, typically 2 to 3 cm away.

Voltage and extracted-current traces for the gun are illustrated in Fig. 2. The current was initiated immediately after application of the gap voltage. The current quickly rose to a level consistent with EGUN predictions, confirming that emission was predominantly from the velvet surface. Over the succeeding 40-ns voltage pulse, the total current reached a value approximately double the space-charge limit. For comparison to the time-integrated measurements, instability analyses were based on the linear current density at the end of the pulse,

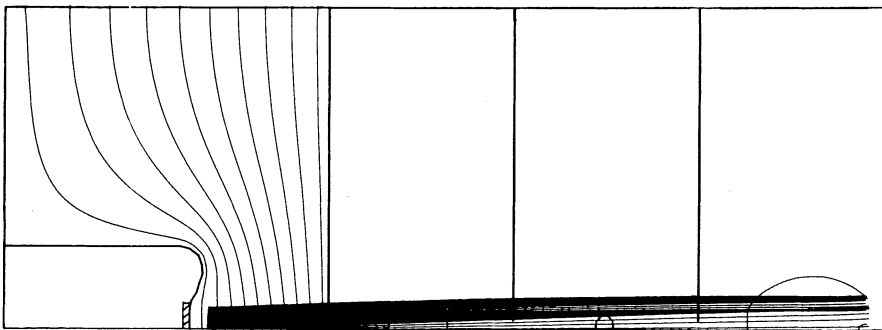SHEET01. 300 kV CHAC sheet beam injector, 1.5 cm gap spacing

FIGURE 8 EGUN simulation, sheet-beam gun with focusing electrode, 1.5-cm cathode-anode spacing, three transport cells 2 cm long. Predicted linear current density: 8.5 kA/m.
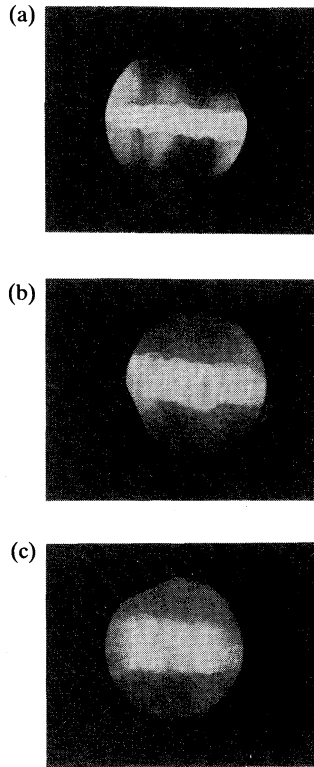
FIGURE 9 Output-beam profiles as a function of distance from anode, sheet-beam gun with focusing electrode, 1.5-cm cathode-anode gap: (a) single transport cell 1.1 cm from anode mesh; (b) dual cell, 3.8 cm from anode mesh; and (c) triple cell, 6.6 cm from anode mesh.

since the gun had the highest power density at this time, and the instability growth rate was predicted to have a maximum value. We measured a linear current density of $J \cong 2 \times 10^4$ A/m at the end of the pulse.

Figure 9 shows a time-integrated beam profile (a) with the scintillator detector located 1.1 cm downstream from the anode mesh. Note the well-defined planar beam with a clear induction of incipient filaments. The full width of the beam was about 0.78 cm, in good agreement with the EGUN prediction. The beam profile indicated that emission took place primarily from the velvet surface, although there were indications of peripheral electrons, probably generated by emission from the focusing electrode. Profiles taken 3.8(b) and 6.6 cm (c) from the anode mesh are also shown in Fig. 9. Measurements of the beam width show an envelope divergence angle of 7°, considerably larger than the EGUN prediction. The increased divergence reflects the combined results of optics mismatch from the cathode plasma expansion and emittance growth from the filamentation instability.

Figure 9 shows a well-developed filamentary structure (a) parallel to the cathode direction observed at very short distances from the anode mesh. The

predicted propagation length for the growth of the filamentation instability from Section 3 is short enough to account for the structure observed. Given the instability growth rate, α, the growth length is approximately.

$$L_g \sim \beta c / \alpha. \tag{16}$$

To estimate L_g, assume that neutralization of transverse electric fields was almost complete near the anode mesh and that the initital emittance of the beam was negligibly small. In the experimental geometry, the distance from the beam to the return-current surface was large compared to the beam width and observed filamentation wavelengths. In this limit, we can take $\tanh(ky_m) \cong 1$ in Eq. (13). With the above approximations, the predicted growth length is

$$L_g \geqslant (2\gamma m_0 \beta c^3 \varepsilon_0 / e J_z k)^{1/2}. \tag{17}$$

Measured values of parameters in Eq. (17) are $\gamma = 1.55$, $\beta = 0.764$, and $J \cong 2 \times 10^4$ A/m. The only other input required is k, the instability wavenumber. This quantity can be estimated from the beam-profile data. A digitization of the intensity profile (a) of Fig. 9 on a line parallel to the cathode surface is shown in Fig. 10. A Fourier analysis shows that the strongest variation occurs with a wavelength of $\lambda = 0.8$ cm. This is a physically reasonable result; in the thin-beam
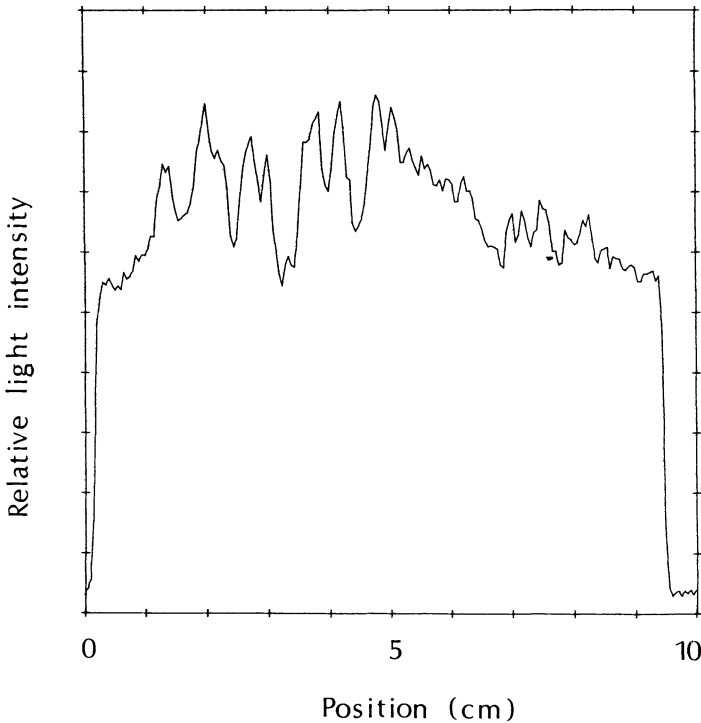

FIGURE 10 Photodensitometer scan of intensity profile of Fig. 9 parallel to long axis of cathode (a).
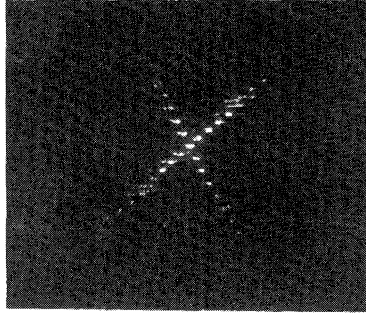
FIGURE 11   Emittance data, sheet-beam cathode with focusing electrode, 1.3-cm cathode-anode spacing, aperture plate 2.4 cm downstream from anode mesh.

limit, Eq. (17) predicts that the strongest filamentation growth occurs at the shortest wavelength. The thin-beam approximation is invalid if the pinching scale length is less than, or comparable to, the width of the sheet beam near the anode. The growth rate for filamentary structures smaller than the beam width is reduced. Consequently, the fastest-growing filaments should have a dimension comparable to, or larger than, the average beam width, on the order of $\Delta y \sim 0.6$ cm. If we take $k = 2\pi/(0.008) = 785$ m^{-1}, Eq. (17) predicts a growth length, L_g, of only 1.4 cm. It is therefore not surprising to observe significant filamentary structure over the total beam-transport length of 2.6 cm.

Emittance data taken 2.4 cm from the anode mesh are illustrated in Fig. 11. The enhancement of the beam angular divergence occurs mainly parallel to the cathode length, consistent with the observed profile (Fig. 10). The divergence in the parallel direction is about 0.11 radians (6.3°), twice the divergence in the normal direction. The downstream divergence has about the same magnitude and becomes more isotropic. The divergence figure can be compared to predictions of Eq. (15) for the saturation angular divergence resulting from filamentation. Inserting parameters for the sheet beam and again assuming complete electrical neutralization and neglecting return current effects gives [from Eq. (15)] a divergence of 0.10 radians (5.7°), in agreement with the observations.

5. CONCLUSIONS

Although foil focusing has been demonstrated as an effective method for high-current electron-beam transport,[10–13] filamentation instabilities set limits on the range of application. To understand the implications of the present results, we must note that transverse conducting foils can serve two functions for beam transport:

1. By reducing transverse electric fields, conducting foils allow a relativistic electron beam to propagate in a self-pinched equilibrium.
2. By lowering longitudinal electric fields and the beam-generated electrostatic potential, conducting foils may facilitate transport of beams at levels beyond the conventional space-charge limiting current.[25]

Transverse focusing by foils is effectively applied to paraxial electron beams propagating below the longitudinal space-charge limit. As an example, the electron beams from linear-induction accelerators envisioned for free-electron-laser applications[26,27] satisfy the paraxial approximation. If the beams are highly relativistic, the required electric-field reduction factor is small, and the foils can be widely spaced. The best strategy for foil transport of such beams is to focus the electrons to an emittance-limited spot at the entrance of the transport array and to arrange the foil geometry so that the beam propagates with a small radius and relatively high angular divergence. The filamentation instability is avoided because the radial-force balance in the foil transport system is dominated by emittance and magnetic forces. Reducing the beam diameter also minimizes emittance growth from foil scattering. Our studies of foil scattering indicate that high-brightness electron beams can be generated by induction accelerators with foil focusing.

The second potential application of foil focusing, propagation of very-high-current (>100-kA) electron beams by the reduction of longitudinal space-charge effects, may be affected by filamentation instabilities. Generation of such beams calls for a high-perveance gun with a grid or foil anode. The present results indicate that there are two related problems associated with this transport geometry:

1. Foils must be closely spaced to achieve a significant reduction in the beam-generated electrostatic potential. Beams entering such a foil array from a high-perveance gun are inevitably over focused. The resulting nonlinear envelope oscillations lead to emittance growth until radial-force equilibrium is attained.

2. High-perveance beams with initially low angular divergence will be subject to the filamentation instability, further increasing the emittance.

If beam brightness is a concern, alternate approaches may be required for very-high-current electron-beam transport, such as an annular beam geometry.

REFERENCES

1. J. R. Freeman, J. W. Poukey, J. S. Wagner, and R. S. Coats, *J. Appl. Phys.* **59,** 725 (1986).
2. G. Benford, *Plasma Phys.* **15,** 483 (1973).
3. C. A. Kapetanakos, *Appl. Phys. Lett.* **25,** 484 (1974).
4. P. J. Christiansen, V. K. Jain and L. Stenflo, *Phys. Rev. Lett.* **46,** 1333 (1981).
5. R. Lee and M. Lampe, *Phys. Rev. Lett.* **31,** 1390 (1973).
6. K. Molvig, *Phys. Rev. Lett* **35,** 1504 (1975).
7. R. C. Davidson, B. H. Hui, and C. A. Kapetanakos, *Phys. Fluids* **18,** 1040 (1975).
8. K. Molvig, G. Benford, and W. C. Condit, *Phys. Fluids* **20,** 7 (1977).
9. G. Benford, *Phys. Rev. Lett.* **28,** 1242 (1972).
10. R. J. Adler, *Particle Accelerators* **12,** 263 (1980).
11. S. Humphries, Jr., *Particle Accelerators* **13,** 249 (1983).

12. R. J. Adler, B. Sabol, and G. F. Kiuttu, *IEEE Trans. Nucl. Sci.* **NS-30**, 3198 (1983).

13. S. Humphries, Jr., and C. Ekdahl, *J. Appl. Phys.* **63**, 583 (1988).

14. J. Ramirez, Sandia National Laboratories, private communication.

15. W. Rogowski and W. Steinhaus, *Arch. Elektrotech.* **1**, 141 (1912).

16. S. Glasstone and R. H. Loveberg, *Controlled Thermonuclear Reactions* (VanNostrand, New York, 1960), 164.

17. J. Cooper, *Plasma Phys.* **5**, 285 (1963).

18. R. J. Adler, G. F. Kiuttu, B. E. Simpkins, D. J. Sullivan, and D. E. Voss, Mission Research Corporation, MRC Report AMRC-N-275 (Albuquerque, 1984).

19. J. T. Weir, G. J. Caporaso, F. W. Chambers, R. Kalibjian, J. Kallman, D. S. Prono, M. E. Slominski, and A. C. Paul, *IEEE Trans. Nucl. Sci.* **NC-32,** 1812 (1985).

20. J. R. Pierce, *J. Appl. Phys.* **11**, 548 (1940).

21. H. R. Jory and A. W. Trivelpiece, *J. Appl. Phys.* **40,** 3294 (1969).

22. P. K. Parker, R. E. Anderson, and C. V. Duncan, *J. Appl. Phys.* **45,** 2463 (1974).

23. See, for instance, C. Lejeune and J. Aubert, "Emittance and Brightness: Definitions and Measurements," in A. Septier, ed., *Advances in Electronics and Electron Physics, Supplement 13A,* (Academic Press, New York, 1980).

24. W. B. Herrmannsfeldt, Stanford Linear Accelerator Center, private communication.

25. See, for instance, R. B. Miller, *Intense Charged Particle Beams* (Plenum, New York, 1982), 90.

26. See, for instance, J. Pasour, *IEEE Circuits and Devices Magazine* **55,** (1987).

27. D. Prosnitz, "Review of Free Electron Laser Theory and Experiments" R. J. Briggs and A. J. Toepfer, Eds., *Proc. 5th Int'l Conf. High Power Particle Beams,* (Physics International Company, CONF-830911, 1983), 540.